Theoretical Models and Qualitative Interpretations of Fs Laser Material Processing

Nadezhda M. BULGAKOVA[1], Igor M. BURAKOV[1], Yuri P. MESHCHERYAKOV[2], Razvan STOIAN[3], Arkadi ROSENFELD[4] and Ingolf V. HERTEL[4,5]

[1] *Institute of Thermophysics SB RAS, 1 Lavrentyev Ave., 630090 Novosibirsk, Russia*
E-mail: nbul@itp.nsc.ru
[2] *Design and Technology Branch of Lavrentyev Institute of Hydrodynamics SB RAS, Tereshkovoi Street 29, 630090 Novosibirsk, Russia*
[3] *Laboratoire TSI (UMR 5516 CNRS), Universite Jean Monnet, 10 rue Barrouin, 42000 Saint Etienne, France*
[4] *Max-Born-Institut für Nichtlineare Optik und Kurzzeitspektroskopie, Max-Born Str. 2a, 12489 Berlin, Germany*
[5] *Department of Physics, Free University of Berlin, Amimallee 14, 14195 Berlin, Germany*

In this paper a number of numerical models are presented which have been developed to describe the processes taking place at different time and length scales in different classes of materials under the irradiation by ultrashort laser pulses. A unified drift-diffusion approach for modeling charge-carrier transport in metals, semiconductors, and dielectrics allows to elucidate the dynamics of the electric field generated in the target due to photo-emission and to get insight into the origin of the Coulomb explosion process. The widely known two-temperature model is used to follow heating dynamics of irradiated matter and to analyze its phase transformations on the basis of thermodynamic concepts. Being modified for semiconductors, this model has allowed to establish the nature of high-energetic ion emission using laser pulse tailoring and to undertake a simplified modeling of consequences of ultrafast melting of silicon. A two-dimensional model of dielectric breakdown has made possible to uncover the mechanisms which enable the spatial modulation of the structures induced by temporally modulated laser pulses in wide-band-gap dielectric materials. A combined thermal/elasto-plastic model has provided a deep insight into the mechanisms and dynamics of the microbump and nanojet formation on nanosize gold films under femtosecond laser irradiation.

DOI: 10.2961/jlmn.2007.01.0014

Keywords: ultrashort laser pulses, drift-diffusion approach, dielectric breakdown, Coulomb explosion, phase explosion, ultrafast melting, elasto-plastic modeling

1. Introduction

Femtosecond laser pulses provide unique possibilities for high-precision material processing. Due to rapid energy delivery, heat-affected zones in the irradiated targets are strongly localized with minimal residual damage that can allow generation of well-defined microstructures with high quality and reproducibility [1]. Understanding of the underlying physics and interrelation of the processes taking place in materials irradiated by ultrashort laser pulses can facilitate optimization of experimental parameters in current applications and development of contemporary pulsed laser technologies. The complexity of the interrelated processes involved in laser-matter interaction gives rise to elaboration of their theoretical and computational descriptions using different approaches.

When ultrashort laser pulse acts on a solid target, a rich variety of physical processes is triggered whose characteristic timescales are presented in Fig. 1. In femtosecond timescale this involves generation of free electrons in dielectric and semiconductor materials [2-4], absorption of laser radiation by free electrons (intrinsic for metals and laser-generated for poorly or non-conducting materials) and, as a result, strong non-equilibrium between the electron and lattice subsystems [5-7], violation of quasineutrality of the target due to electron photo-emission (PE), possibilities of Coulomb explosion (CE) in dielectrics [8,9] and ultrafast melting of semiconductors [10,11,12]. Electron-lattice temperature relaxation and normal (or, in the other words, thermal) melting occur from several to hundred picoseconds after irradiation, depending on the material properties. As a result, melted material can reach a metastable state and, under definite conditions, material ablation via phase explosion (or explosive boiling) takes place [13-16]. Plastic deformations can be caused by the thermal stresses in both thin films and bulk materials due to high temperature gradients [17-20]; however they are developed in ns-timescale, as well as significant cooling with resolidification, because of their low velocities of order 10 – 100 m/s. Many of the processes listed above are in a strong correlation and can be described only jointly. Thus, Coulomb explosion modeling involves description of free electron generation, their heating and photo-emission, and, as a result, generation of the self-consistent electric field and electric current in the targets [21]. At the same time, the analysis of dielectric heating and ablation can be performed with a good accuracy without considering the

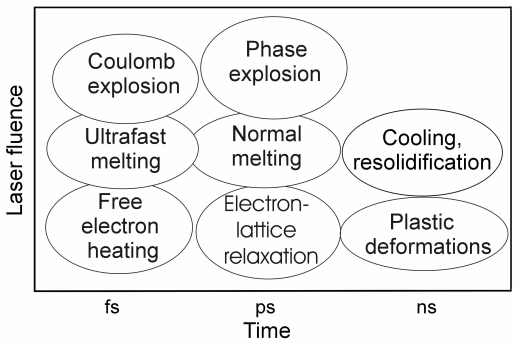

Fig. 1 Schematic representations of timescales for response of different materials to the femtosecond laser excitation (see explanations in the text).

PE process and its consequences [22]. Due to the fact that some of the processes induced by fs-laser in solids are alternating in time [23], their description can be simplified by changing the governing sets of the equations during modeling procedure. Thus, much can be learned about the material behavior with the use of the two-temperature model (TTM) giving way to the single heat-flow equation for the bulk material and the gasdynamic equations for the superficial target layer as soon as electron-lattice temperature equilibration was reached [14]. More accurate description should include through calculations of the ablated and non-ablated parts of the target [24,25] though this task is extremely complicated. Another example of successful modeling of the alternating processes is the description of laser-induced plastic deformations whose development is strongly delayed in respect to heating [20].

In this paper we give a review of a number of models developed previously by the authors to describe material response to the action of ultrashort laser pulses. The paper is organized as follows. In Section 2 we discuss the processes leading to Coulomb explosion of dielectrics, introduce the CE criterion, and give a comparative analysis of different types of materials in respect to charging the laser-irradiated surfaces. Section 3 is devoted to the analysis of the thermodynamic state of melted matter from the viewpoint of ablation via phase explosion. In Section 4, we introduce a two-dimensional (2D) model of dielectric breakdown which makes possible to uncover the mechanisms enabling the spatial modulation of the structures induced by temporally modulated laser pulses in the wide-band-gap dielectric materials. Finally in Section 5, the combined thermal/elasto-plastic model is presented which provides insight into the mechanism of microbump and nanojet formation on nanosize gold films under femtosecond laser irradiation.

2. Coulomb explosion: causes and effects

Powerful laser irradiation of all kinds of bulk materials causes considerable electron photo-emission from the target surfaces [26]. This leads to the charging of the irradiated sample surface, quasineutrality breakdown in the irradiated targets as a whole and, as a result, to generation of the electric field. For the case of dielectrics, the spike of the electric field can be as strong as 10^{11} V/m and exists up to 1 ps [8] that should result in material disintegration via CE mechanism. Addressing the subject of Coulomb explosion, we imply removal of at least several monolayers [8,21] but not electrostatic desorption, which is of stochastic nature and results from localization of electronic excitation energy at specific atomic sites [27].

2.1 Criterion of Coulomb explosion

Coulomb explosion can be realized when the energy of the electric field generated in the target or applied from outside exceeds the binding energy of atoms (or larger pieces composing matter like molecules or clusters) in the bulk material. For surface atoms the binding energy can be evaluated from the latent heat of vaporization corresponding to one atom Λ_{at} [21,28]. Comparing the value of the binding energy with the energy of the electric field corresponding to the volume occupied by one atom, we obtain the threshold electric field with respect to CE:

$$E_{th}\,|_{x=0} = \sqrt{2\Lambda_{at} n_0 / e e_0} \qquad (1)$$

where n_0 is the number density of the target material. For sapphire we obtain $E_{th} \sim 5 \cdot 10^{10}$ V/m whereas for gold and silicon the estimated threshold electric fields are smaller, $2.76 \cdot 10^{10}$ and $2.65 \cdot 10^{10}$ V/m respectively. It should be noted that the heated surface atoms having a definite energy of vibrations can escape from the surface with higher probability than the cold ones, a fact which should decrease the above threshold value [21,28]. Also the surface adatoms having lower binding energy with the surface as compared to usual surface atoms can be emitted at even lower electric field. However, for macroscopic CE when at least several monolayers of material are ablated, Equation (1) represents a reasonable criterion.

2.2 Experimental evidence for Coulomb explosion

Coulomb explosion has been proven experimentally [8,9,29,30] to occur in dielectrics under femtosecond laser irradiation with 800-nm laser wavelength. It should be underlined that the above observations were performed at laser fluences only slightly above the ablation threshold (note that for the Coulomb explosion regimes, conditions may be created where ion emission can be initiated below the thermodynamic melting threshold, due to the different nature of the corresponding mechanisms). With increasing laser fluence beyond the onset of thermal mechanisms involving melting and vapor transformation, the additional mechanisms of rather thermal nature are superimposed on CE and can substantially mask the latter. The main difference of the electronic and thermal mechanisms is in scaling of the velocity distribution of species which is momentum scaling for the first and energy scaling for the second. On the one hand, higher laser fluence induces stronger electron photo-emission, thus enhancing CE probability. But on the other hand, the particles abundantly emitted during phase explosion have a wide velocity distribution with a high-energy tail masking the electronically ablated energetic particles. Another masking factor can be charge separation in the gas phase that leads to appearance of a high-energy ion peak in the front of the plume with momentum scaling in the velocity distribution [31,32]. Observations of CE at high laser fluences well above the ablation threshold are thus contradictory as it can involve a number of the superimposed mechanisms leading to the same effect of fast particle generation [33,34].

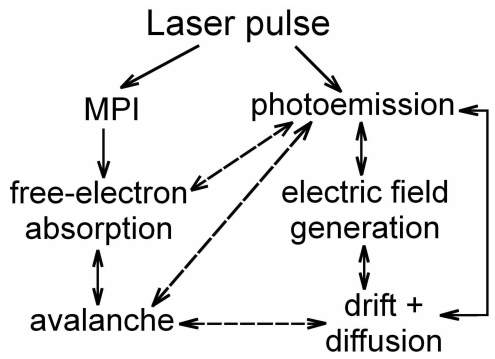

Fig. 2 A scheme of major interconnections between different processes.

2.3 Surface charging: Formulation of the model

The theoretical description of carrier dynamics in different kinds of materials under short pulsed laser irradiation is a complicated task implying consideration of a broad spectrum of the interrelated processes. A laser pulse impinging on a target triggers a sort of avalanche of the processes swelling with time or being damped. Some of them give rise to the other processes; these are in strong interconnection, which is demonstrated in a simplified scheme shown in Fig. 2 for the case of dielectrics and semiconductors. Roughly, the processes can be divided in two branches: one starting from photoionization (with the order of the process depending on the relation between the photon energy and the material bandgap) and another starting from photo-emission (with the order of nonlinearity determined by the ratio of the work function to the photon energy). Dependences between different processes are shown by arrows. Most of the processes are interconnected that is shown by double-sided arrows. Dependences of the processes within a branch are stronger (solid lines) than between the branches (broken lines).

The electrons excited to the conduction band absorb laser radiation and can produce secondary electrons by collisional ionization. As soon as electronic avalanche is developed, absorption and reflection dynamics vary dramatically. A drastic consequence of electron photo-emission is the violation of the target quasi-neutrality that results in positive charging of the target as a whole and thus in generation of an ambipolar electric field. The electric field forces the charge carriers to relocate in order to neutralize the excess positive charge. The charge-carrier current is a superposition of drift and diffusion. Redistribution of the charge carriers (free electrons and, in the case of semiconductors, holes) affects electron photo-emission and the avalanche multiplication process. Photo-emission depletes a superficial target layer breaking further development of collisional multiplication in this region and, in turn, avalanche regulates photo-emission through its influence on the available free-electron density. On laser pulse termination, recombination of free-carriers occurs through Auger recombination in semiconductors and a trapping-like phenomenon in dielectrics (not shown in the scheme).

The described processes can be simulated under the following assumptions [21,28]. The continuity equations for electrons and holes (ions) is written in a general form as

$$\frac{\partial n_x}{\partial t} + \frac{1}{e}\frac{\partial J_x}{\partial x} = S_x + L_x \qquad (2)$$

where S_x and L_x are the source and loss terms describing the free carrier populations, n_x denotes the carrier densities with subscript $x = e, i$ representing electrons and ions respectively, J_x is electric current consisting of the drift and diffusion terms. Note that our model is one-dimensional that is justified by enhanced transversal lateral dimensions for the laser spot with respect to the absorption depth. The source term accounts for free electron generation (one- or multiphoton ionization depending on the material band gap and avalanche). In the loss term, free-carrier recombination is taken into account as well as loss of electrons in volume photo-emission from the electronic escape depth. In metals and semiconductors, we consider photo-emission as a surface process and the PE term is set as a boundary condition for electric current through the sample surface [21,28]. For metals, Equation (2) has a zero right part.

Electric field generation resulted from PE is described by the Poisson equation. It should be noted that, even in absence of PE, the internal electric field can be found in dielectrics and semiconductors due to strong density and temperature gradients of charge carrier population [35] (with preserving quasineutrality of the target as a whole). On the other hand, the calculations show that PE and surface charging influence only slightly the energy balance without noticeable impact on the damage and melting thresholds, a fact which justifies the use a wide variety of models describing laser light absorption and heating of different kinds of materials.

The energy balance in the target is described by using the TTM for metals [5-7] and a TTM-like model for semiconductors and dielectrics [21,28], assuming that strongly ionized insulators and semiconductors can be considered as dense plasmas. Even if complete equilibration does not take place in the electron and lattice subsystems, their temperatures can be considered as measures for the average energies.

Attenuation of the laser power inside the dielectric and semiconductor targets is determined by the loss mechanisms involving free electron generation and by the optical response of a collisional free-electron plasma and the vacuum-plasma interface through the Fresnel formulas. The complex dielectric function can be seen as a mutual contribution of the unexcited solid and the response of the laser–induced free electron gas [36]. We do not present here the whole set of the governing equations and refer the readers to Refs. [21,28].

2.4 The result of model application to Au, Si, and Al_2O_3

As modeling systems for three kinds of materials, we have chosen gold, silicon, and sapphire for which a plenty of material data exists in the literature. To test the model, the damage thresholds for these materials were firstly calculated and compared with previously published data. The test for Au was performed for a bulk sample irradiated by 200 fs laser pulse with the wavelength of 400 nm [7]. Melting is reached at *absorbed* fluence of 130 mJ/cm^2 that

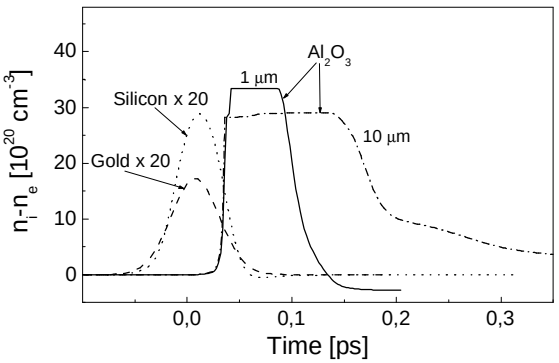

Fig. 3 Temporal behavior of the net surface charge density (the difference between the hole and electron populations) for different classes of materials. Laser fluences are chosen to be above the ion emission threshold for each material (4 J/cm^2, 0.8 J/cm^2, and 1.2 J/cm^2 for Al_2O_3, Si, and Au, respectively). The laser pulse of 100 fs duration is centered at $t = 0$.

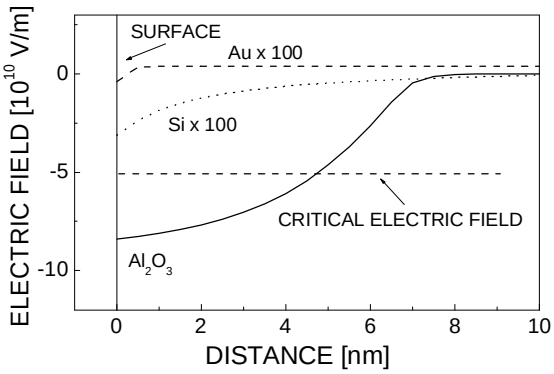

Fig. 4 Spatial bulk profiles of the electric field induced by ultrafast laser radiation in metals, semiconductors, and dielectrics at time moments of reaching the maximum values of the electric field for every material. Irradiation conditions are as in Fig. 3.

is in a reasonable agreement with experimental observations. The calculated damage thresholds for Si and sapphire at 800 nm wavelength take place when an electronic density in excess of the critical value (similar to $1.74 \cdot 10^{21}$ cm^{-3}, the critical density for a free electron gas in vacuum in interaction with 800 nm radiation) is reached, at 0.3 and 2.7 J/cm^2 respectively, also in good agreement with the experimental studies [37,38]. Considerable electron depletion of the surface layer of the sapphire target leads to a slight shift of the breakdown region toward the bulk (of the order of the electronic escape depth). According to the calculations for 800 nm and 100 fs laser pulse duration, the Si sample reaches the melting temperature also at around 0.3 J/cm^2.

In Figure 3 the dynamics of the net positive charge accumulated on the surface for materials studied are plotted as a function of time for laser pulses of 100 fs duration at 800 nm wavelength. The laser fluences are chosen to be slightly above the experimental ion emission thresholds [7,36-39], namely 4, 0.8, and 1.2 J/cm^2 for sapphire, silicon and gold respectively. Under these specific irradiation conditions the electronic temperature reaches considerable values ranging from around 1 eV in gold to approximately 6 eV in silicon and more than 10 eV in sapphire. It is obvious that the net charge is significantly higher for the dielectric target than for the metal or for the semiconductor target. For sapphire the results are given for two numerical regions of 1 and 10 μm to illustrate the importance of the position of the remote boundary which allows electron supply from the material depth. The position of the remote boundary is important also for silicon while for metals the depth of the numerical region can be as small as 2-3 skin-layer widths. The size of 10 μm corresponds to the irradiated spot radius in the experiments [8,29] and indicates the upper limit of the one-dimensionality assumption. Increasing the numerical region from 1 to 10 μm results in an insignificant reduction of the maximum charging (about 10%) with an approximately double increase of the charging period.

It should be particularly emphasized that strong charging of sapphire (Fig. 3) is not a result of higher photoemission as compared to silicon and gold. According to modeling, the photoemission yield is approximately $6.8 \cdot 10^8$ electrons for the sapphire target over the whole laser pulse duration from an irradiated spot of 470 μm^2, whereas $6.2 \cdot 10^{11}$ and $3.5 \cdot 10^{11}$ electrons are removed from the Si and Au targets, respectively.

The calculations show that the electric field generated on the target surfaces experiences sharp spike and then rapidly decreases because of the relocation of the charge carriers within the target. The maximum electric field generated in sapphire exceeds the critical value and reaches $8.4 \cdot 10^{10}$ V/m beneath the surface. The above-threshold electric field exists for a few tens of fs. The maximum values of the electric field are only 4.1×10^7 V/m and 3.4×10^8 V/m for gold and silicon respectively. The spatial distributions of the electric field in the near-surface layers are given in Fig. 4 for time moments when the field has reached its top value. The negative value implies that the field is directed away from the target, streaming from the sub-surface layers to the vacuum. For sapphire, the layer with overcritical electric field where electrostatic disintegration of the lattice should occur is approximately 40 Å wide, in excellent agreement with the experimental estimation of the Coulomb exploded region [8]. Thus, we have demonstrated that, under studied conditions, *slightly above the material removal thresholds*, charging of dielectric surfaces causes Coulomb explosion, while this effect is strongly inhibited for metals and semiconductors. Below we shall show that the unified continuum approach developed for modeling the dynamics of electronic excitation, heating and charge-carrier transport in different materials under fs pulsed laser irradiation can be applied for a wide range of the problems concerning ultrashort laser – material interaction.

3. Phase explosion under ultrashort laser ablation

The laser-induced processes leading to material ablation are strongly dependent on the material properties and can be sufficiently different or proceed differently in different classes of materials [23]. In *metals*, laser energy is absorbed by free electrons via the inverse Bremsstrahlung process in a skin layer of order of 10 nm. The electron-electron relaxation rate depends on the energy accumulated in the electron gas during laser heating [40]. In the regimes

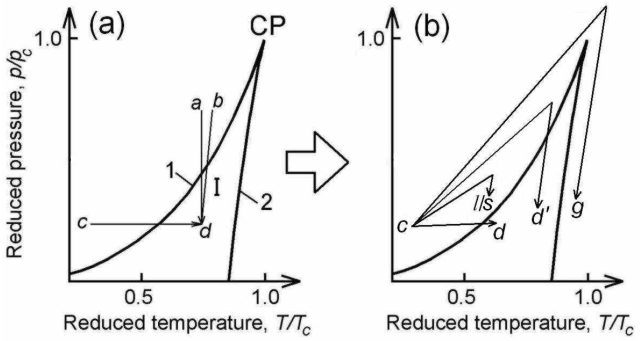

Fig. 5 (a) Typical *p-T* phase diagram: 1 is the binodal; 2 is the spinodal; CP is the critical point. The region I between binodal and spinodal corresponds to the metastable states of matter. Lines *ad*, *bd*, and *cd* illustrate the different ways to get into a metastable state *d*. Adapted from Ref. [41]. (b) Sketch of the evolution roads illustrating fs laser irradiation regimes (see text).

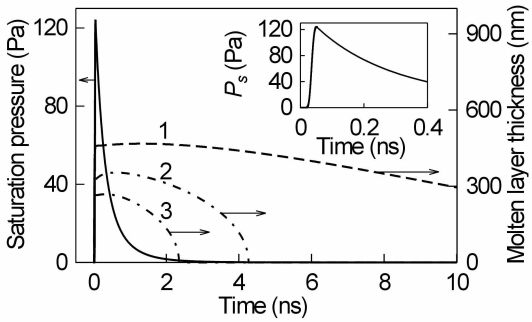

Fig. 6 The thickness of the molten layer (dashed line) and saturation pressure calculated using the surface temperature (solid line) as the functions of time after irradiation of a golden target by a 200 fs, 0.4 J/cm^2 laser pulse. The inset shows the saturation pressure with higher resolution.

resulted in metal melting and ablation, when the internal energy of the electron subsystem reaches several eV per electron thus exceeding 10^{10} J/m^3, the electron gas can be considered as thermalized (see Fig. 9 in Ref. [40]) and the TTM [5-7] is valid on the timescales relevant for femtosecond laser pulses. Electron-lattice relaxation requires longer times, in the range of 10 - 100 ps [7] and this time is much shorter than the characteristic time for establishing stationary distributions of the parameters in superheated liquids (hypothetical time is ~1–10 ns [41]). Even for nanosecond laser pulses, heating can be extremely rapid at high laser fluences so that the melted material experiences superheating that results in phase explosion as the main mechanism of ablation [13,42]. At shorter, picosecond and femtosecond laser pulse durations, a fast solid – vapor/plasma transition may take place [1] with the possibility to drive the superheated matter into a metastable state culminating with phase explosion [14,43].

In the *p-T* diagram (Fig. 5a), the different ways to get into a metastable state *d* are shown [41]. The line *ad* corresponds to isothermal decreasing of the pressure and the line *cd* shows isobaric heating. Due to small compressibility of the liquid, the line of adiabatic expansion *bd* is close to *ad* (the effect of adiabatic cooling is small). Applied to ultrashort heating like under the fs laser irradiation conditions, the heating scheme should be modified (Fig. 5b). Roughly, line *cd* corresponds to the evolution of a thin external target layer adjacent to vacuum or ambient atmosphere for a case when ablation threshold is not reached. The deeper layers have more complicated trajectories in the phase space depending on the electron-lattice coupling rate and the velocity of the unloading wave. Heating of a layer leads to synchronous pressure rise with subsequent adiabatic unloading. Different layers evolve to the different thermodynamic states, being superheated in to a metastable state (*c – d'*), or heated to a stable state with melting and subsequent solidification (*c – l/s*) or drawn into a gaseous phase above the critical point (*c – g*). The evolution trajectories shown in the Figure for simplicity by the straight lines can be quite intricate [16]. First approximation for estimations of superheating degree can be performed with the use of the TTM [5-7,14]. Being widely used, the model has not exhausted its potentialities, particularly in simulating highly non-equilibrium behavior of matter on a rather qualitative level. The combined TTM – molecular dynamic (MD) [44] or Monte-Carlo – MD [16] approaches have a great potential for getting deeper insights into dynamics of ultrafast laser excitation of different kinds of material. However it should be mentioned that, for strongly non-equilibrium matter containing the electrons as degrees of freedom, the MD technique has to be based on the many-body potential energy surface simulations taking into account occupations of the electronic levels in the valance band as well as free electron contribution [45]. The models based on an interatomic potential such as the Lennard-Jones, Tersoff, or Stillinger-Weber do not allow reasonable description of ultrashort structural changes [45].

3.1 Metals

Here we give two examples which illustrate the two different thermodynamic pathways of material superheating after ultrashort laser irradiation. A qualitative analysis is based on application of the TTM to describe heating a gold sample by femtosecond laser pulses with 400 nm wavelength. Further evolution of the heated target is described by the single thermal conductivity equation and, if the temperature in the external target layer exceeds T_c, the Euler equations govern the dynamics of the vapor layer. For simplicity the thermodynamic critical temperature T_c is used as the vapor – liquid interface criterion, according to the definition of the critical point (CP). This choice is determined by the fact that the CP is a state of substance in which the potential energy of mutual attraction of the molecules is equalized to some extent by their average kinetic energy. When a substance is heated above the critical temperature, it starts to expand in a quasi-free manner. The Euler equations were supplemented by the generalized van der Waals equation [46], which describes adequately the state of metals in the CP vicinity, and by the corresponding caloric equation.

As mentioned, *cd* in Fig. 5 corresponds to the external target layer in the case when the ablation threshold is not reached. This case is illustrated in Fig. 6 where the position of the liquid − solid interface and the corresponding saturation pressure P_s vs. time for incident laser fluence of

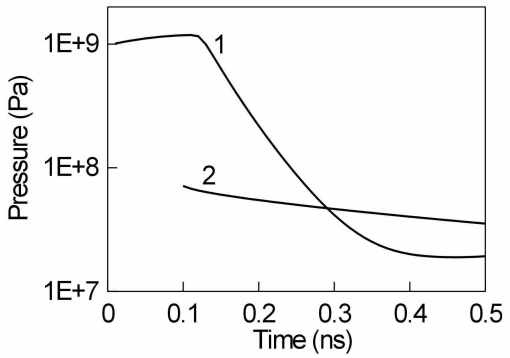

Fig. 7. Temporal behavior of the pressure above the molten surface in vapor phase (1) and the saturation pressure calculated by the temperature in liquid – vapor interface (2) for the case of a 200 fs, 1.65 J/cm^2 laser pulse.

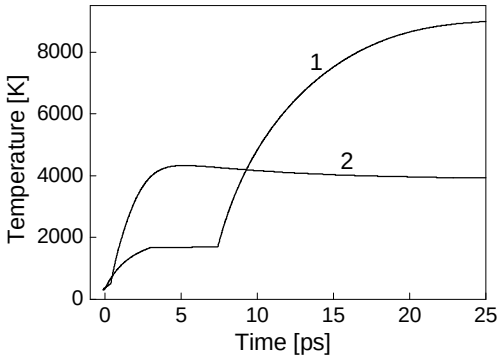

Fig. 8. Temperature temporal profiles on the surface of the excited silicon sample during the optimal irradiation sequence (1) and after the single pulse (2).

0.4 J/cm^2 are shown. In the timescale of order of 1 ns, the unloading wave travels through the melted layer. For this timescale, by comparing P_s with the ambient pressure, one could infer the extent to which the liquid metal is superheated to the region I (Fig. 5), implying that the pressure above the surface is not changed due to strongly delayed thermal vaporization. The higher the ambient pressure is, the thinner is the superheated liquid layer and the shorter is the time of metastability. In Figure 6, the thickness of the superheated liquid layer is shown for the ambient pressures of 0.1 Pa (line 2) and 1 Pa (line 3), while in deep vacuum whole melted layer is metastable. Superheating degree is not large in these cases. Its maximum is reached by the time of the electron–lattice temperature equilibration (see inset in Fig. 6), whereupon P_s decreases exponentially with the surface temperature decrease. In this situation, phase explosion is unlikely. However, ablation can be triggered e.g. by irradiation of the surface by a second, correspondingly delayed, laser pulse (also below the ablation threshold). This apparently takes place in the pump–probe experiments [47]. The peak of emitted ions observed in [47] for the picosecond range of the pump–probe delays corresponds presumably to maximum superheating.

The case corresponding to the paths *cg* for the external target layer heated to a supercritical state and *cd'* for the liquid layer adjacent to the liquid – vapor interface (Fig. 5) is illustrated in Fig. 7 (incident laser fluence of 1.65 J/cm^2). In this case, the vapor layer 600 Å thick expands freely into vacuum. As shown in [48], the effective material stress in the gold target can reach several GPa. The vapor pressure above the molten layer decreases rapidly, thus dropping below the saturation pressure of the melt. For fairly high laser fluences, the recoil pressure of expanding vapor may play a role of the external action, inducing phase explosion as it likely took place in the experiments [49]. The value of the recoil pressure initiating explosive boiling invites further investigations. It should be noted that the choice of the critical temperature or another temperature level (e.g. 0.9 T_c [13]) as the ablation criterion does not influence the main conclusion of this analysis which is, during expansion, the pressure of the ablation products falls below the saturation pressure of the underneath melt.

3.2 Semiconductors

It is interesting that, with adaptive pulse temporal tailoring, by redistributing laser energy in the irradiation sequence, one can control the thermodynamic paths for the evolution of the irradiated matter [50]. In Ref. [50], the possibility to optimize the kinetic characteristics of ions emitted from laser irradiated semiconductors was demonstrated. This technique can be also used for more efficient material processing.

We have made an attempt to describe heating of silicon irradiated by the tailored laser pulses with 800-nm wavelength in order to provide insight to the possibilities of manipulating the emitted ion beams [50]. A silicon target was irradiated with the single (170 fs duration) and tailored laser pulses with the same total energy $E_L = 4E_{th}$ (E_{th} is the melting threshold energy). The tailored pulse consisted of a prepulse of 170 fs duration with the energy E_{th} while the rest energy was deposited in a Gaussian picosecond pulse of 7 ps duration whose maximum was delayed by 7 ps with respect to the prepulse. We use the continuum approach presented in Section 2, disregarding the charge-carrier transport as it affects lattice heating to a minor extent [28]. Heat flow in molten silicon is treated similar to ductile metals [50]. In the calculations the total laser fluence was scaled to the numerical melting threshold (Section 2: E_{th} = 0.3 J/cm^2, a slightly higher than reported experimentally).

The temporal evolution of the temperature in the target surface layer for the case of the tailored pulse is presented in Fig. 8, line 1. Three distinct regions can be identified: the quasi-isochoric lattice heating by electron-lattice energy exchange after the first pulse, the constant plateau where energy is supplied as latent heat of fusion and the liquid phase is nucleated, followed by further heating of the molten layer. Kinetic limitations for equilibrium boiling, which involves bubble formation and diffusion, create the conditions for impetuous heating of matter. As a result, the liquid layer is pushed into a supercritical fluid state [51] (T_c = 5160 K). The supercritical fluid exposed to the second pulse decomposes into a gas mixture as a result of the nearly adiabatic expansion above or across the spinodal [52]. The energy density stored in the liquid phase in different regions below the surface is the critical parameter that defines whether mass transfer occurs via homogeneous nucleation of gas bubbles [51] or, as in our case, the

supercritical fluid will rapidly decay to the gas phase without forming critical vapor nuclei. Redistributing the energy in the irradiation sequence can scan the whole ensemble of thermodynamic paths. The supercritical expansion reaches, for the decomposed fluid, velocities in the range of 10^4 m/s [52]. Collisional equilibration and further charge separation during plume expansion will accelerate the ions beyond this value. In contrast, a single short pulse with a total energy of $4E_{th}$ induces, notwithstanding the fast appearance of the liquid phase, a 65% reduced temperature which saturates below the critical point (line 2 in Fig. 8), indicating phase explosion as the most probable transition to gas-phase.

3.3 Ultrafast melting

Ultrafast (UF) excitation of semiconductors at fluences above the damage threshold proceeds through a highly reflective, metal-like phase upon the development of a dense, overcritical electron-hole plasma [36] with the optical response of a free electron gas. If a significant percent (~10-15%) of the valence electrons is pumped in the conduction band, the strong electronic excitation is almost immediately followed by bond softening and a sharp reduction of the average bonding-antibonding splitting, lattice destabilization, and the appearance of non-thermal phase transitions (UF melting) on a sub-ps time scale [10,11,12]. Here, without entering into atomistic considerations, we will discuss the potential consequences of UF melting on the ablation process.

A fast phase transition, implying a sharp change in the free electron population and carrier transport properties in a confined semiconductor surface layer or, in case of homogeneous nucleation, in islets of liquid phase, results in extremely steep gradients of the free electron density. This is an insurmountable obstacle for the direct application of the drift-diffusion approach (Section 2). However, we undertook a simplified *qualitative* modeling, disregarding electron photoemission and charge-carrier transport. This is partially justified by the fact that the laser-induced disordered phase has a metal-like nature, with high electronic densities, while the carrier mobility (~1 $cm^2/V{\cdot}s$) lies well below the usual carrier mobility in ductile metals.

Modeling was performed for 800 nm laser pulses of 100 fs duration with the fluence ranging from 0.6 to 5 J/cm^2. The parameters of interest were the thickness of the UF melted layer and the average electron energy when the band gap collapse occurs. UF melting was assumed to be triggered in a numerical cell (5 Å thick) when approximately 10% of the valence electrons ($2{\cdot}10^{22}$ cm^{-3}) have been excited to the conduction band. During the next 400 fs [11] (fixed for every numerical cell) required for the completion of the ultrafast order-disorder phase transition, the silicon behavior follows the excited solid dynamics and then the properties of liquid silicon are switched on instantaneously, considering that all initial valence electrons belong now to the conduction band [53].

The results of these simplified calculations are presented in Fig. 9. According to our modeling, UF melting starts at ~0.65 J/cm^2, 2.2 times higher than the thermal melting threshold (see Section 2) that is in reasonable agreement with the experimental observations [11]. The depth of the non-thermally melted layer is 20–40 nm in the fluence

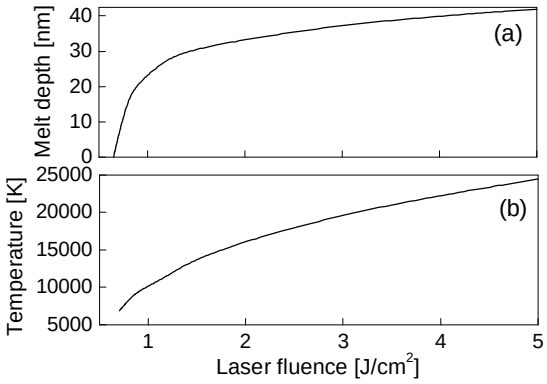

Fig. 9. The depth of the non-thermally melted layer (a) and the average temperature of the electrons immediately after band gap collapse (b).

range of 1–5 J/cm^2 (Fig. 9a) that is also consistent qualitatively with observations involving time-resolved X-ray diffraction on the melting dynamics [11]. It should be emphasized that thermal melting, which inevitably takes place after UF disordering following the dissipation of the energy confined in the electronic system, occurs much faster in the high fluence regime than at low fluences, below the UF melting threshold, and a ten times thicker molten layer develops below the target surface. The temperature of the electrons after band gap collapse (this quantity here is a measure of the average electron energy) increases from ~0.5 to more than 2 eV in the fluence range of 0.6–5 J/cm^2 (Fig. 9b). Under these conditions, the Debye length is of the order of one monolayer (~2 Å). However, in view of intensive photoemission, breaking the quasineutrality at the Si surface can take place in a wider region. In addition, electron thermalization takes additional time. One can expect that, immediately after the band gap collapse, the distribution function of the electrons consists of a cold electron core and a high-energy tail (>10% of electrons with $E_e \geq 10$ eV). Such a situation should lead to a strong double layer effect [32] at the semiconductor surface and may, presumably cause Coulomb explosion.

The same situation (strong gradients of electron density, non-equilibrium distribution function) should exist in the bulk depth during the homogeneous nucleation of the liquid phase [54]. At the boundaries of the liquid phase nuclei [44], in very narrow regions around the liquid islets, a double layer effect can influence strongly the motion of the liquid phase boundary. It should be underlined that this effect is expected to be much stronger for ultrafast excitation, when electron energies are high, than for longer pulses, when the electron and lattice subsystems can be considered to be in equilibrium. A more detailed picture of heating, melting, and ablation of semiconductors can be obtained by application of the molecular dynamic techniques [45] which can provide insight into the fluctuating nature of ultrafast phase transformations including homogeneous nucleation of the liquid phase in solids and, probably, double layer effects.

4. Material modification using temporally shaped femtosecond laser pulses

Temporal tailoring of ultrafast laser pulses allows delivering energy to the irradiated solid in a sequence

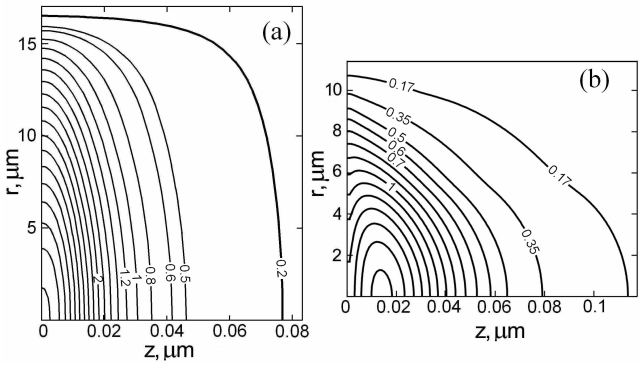

Fig. 10. Simulated lattice-temperature contour maps obtained for Al_2O3 (**a**) and a-SiO_2 (**b**) samples after the action of a triple train of identical pulses (1-ps separation) with 100-fs duration and a total fluence of 14 J/cm2 at 3 ps after the maximum of the first pulse. The temperature levels are marked in eV.

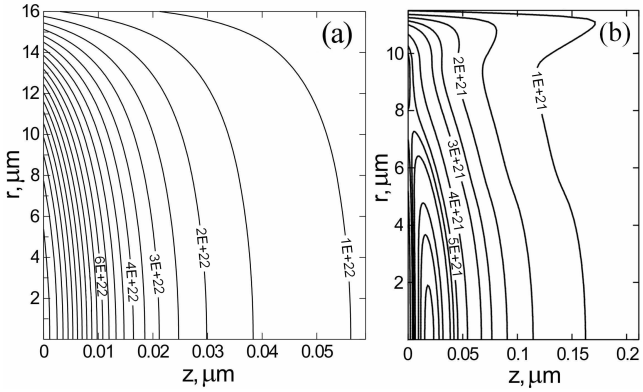

Fig. 11. Electron-density contour maps for Al_2O_3 (**a**) and a-SiO_2 (**b**) samples for the same irradiation conditions as in Fig. 8 at 2.2 ps after the maximum of the first pulse. The contour-map levels are marked in cm^{-3}.

synchronized with the characteristic response of the material. When dielectric materials are exposed to modulated laser radiation, the sequential energy delivery may induce a preparation of the surface (i.e. defined electron density and phonon temperature) and associated material softening during the initial steps of excitation, thus changing the energy coupling for the subsequent steps. This may lead to lower stress, cleaner structures, and provides a material-dependent optimization process, with clear benefits especially for brittle materials [55]. Understanding the underlying physics and the interrelation of the processes taking place in dielectrics irradiated by temporally tailored pulses can open additional ways for optimizing and controlling microprocessing technologies. Here we present a modeling approach aimed to describe the mechanisms that enable the spatial modulation of the structures induced by temporally-modulated laser excitation and ablation of wide band-gap dielectric materials. As modeling systems, we have chosen two types of dielectric materials with different characteristics in relation to the electron-phonon coupling strength, fused silica and sapphire.

The description of the energy absorption and transport in dielectrics under the action of temporally shaped laser pulses is based on the one-dimensional approach presented in Section 2 and developed to the 2D case. This implies cylindrical symmetry for the problem of laser excitation. The 2D extension is motivated by the direct comparison to experimental spatial profiles of laser induced craters [22,55]. The effects of surface charging and the associated ambipolar electric field are ignored as affecting lattice heating insignificantly [28].

Thus the model is based on solving the similar equations as listed in Section 2, written in the 2D form. Charge-carrier transport is disregarded so the Poisson equation is excluded from modeling. The detailed description of the modeling equations with the characteristic parameters is presented in Ref. [22]. The modeling was performed for the specific experimental conditions [55] where the possibility of modulating the spatial depth profile as a function of the pulse separation in the excitation sequence was demonstrated. In the experiments, no modulation is observed in fused silica with short separation, while increased temporal distances between pulses result in a tendency toward a step profile. Similar irradiation of sapphire has produced no modulation. It was supposed [55] that carrier trapping is responsible for observed difference in the crater shapes produced in these two materials [37,56].

Figure 10 presents the contour maps of the lattice temperature in sapphire (a) and fused silica (b) generated after the action of a triple laser pulse with separation between pulses of 1 ps (the time is counted from the maximum of the first pulse in sequence). The contour lines of the lattice temperature in the sapphire sample have a smooth oval form (Fig. 10a). In fused silica (Fig. 10b) a certain modulation of the temperature contour lines is developed with a hollow in the center of the irradiation spot, evidently having common features with the crater forms observed in the experiments [55]. In modeling with smaller time separation between pulses of the order of several hundred femtoseconds, the geometry of contour lines for both materials was similar to that shown in Fig. 10a without signs of spatial modulation.

As proven in Section 2, at laser fluences above the ablation threshold dielectrics can experience Coulomb explosion that results in removal a surface layer several dozen Angstrom thick. However, most of the material is removed following a phase transition (as discussed in Section 3), so namely temperature contour lines should be used as a criterion to evaluate the crater geometry. A certain part of the excited material in a surface target layer situated in the middle of the irradiation spot (Fig. 10) is evidently heated above T_c. To evaluate T_c, one can use one of the methods discussed in Ref. [42]. For majority of materials, an expected value of T_c is 1.5-2 times higher than the boiling temperature under atmospheric pressure which is 2270 K for SiO_2 and 3250 K for Al_2O_3 [57]. So, expected T_c is around 4000 K for fused silica and between 5000 and 6000 K for sapphire. According to thermodynamic concepts [14,41,42], a liquid matter rapidly heated close to T_c experiences strong superheating and decays into vapor and liquid droplets through explosive boiling (phase explosion). Moreover, in extremely fast processes like

ultrashort laser ablation, the superheated liquid and supercritical fluid matter can cross the spinodal and decay into the gas phase without the formation of the critical vapor nuclei [57]. As a rough guide, a liquid zone with the temperature above T_c should be ablated through spinodal decomposition, forming a crater shape corresponding to a "critical" contour of the lattice temperature, ~0.5 eV for sapphire and ~0.35 eV for fused silica (Fig. 10). Comparison of Fig. 10 with the experimentally observed structures [55] shows that the corresponding "critical" contours are in good qualitative agreement with the experimental data on crater geometries.

What are the factors that intervene in the crater spatial modulation? The answer becomes evident from Fig. 11 where the contour maps of the free electron density are presented for the cases shown in Fig. 10. In the sapphire sample (Fig. 11a), due to slow trapping dynamics, the maximum of free electron density generated in the course of the pulse sequence action is located on the target surface in the middle of the irradiation spot, leading to enhanced laser energy absorption in this region and, correspondingly, to increased lattice heating. One can see obvious conformity of the contour maps of the temperature and free electron density (Figs. 10a and 11a). In fused silica (Fig. 11b), the contour map of the free electron density is more complicated. Because of the rapid trapping process [54], the surface layer in the middle of the irradiation spot is depleted of free electrons, so that the maximum of the free electron density is shifted toward the bulk and toward the irradiation spot periphery. Remarkable is the formation of a ring of the free electron density in the surface layer with its maximum located in the irradiation spot periphery. Hence modulation in free electron density distribution and associated laser energy absorption cause modulation of lattice heating and ablation.

Thus, we have demonstrated a modeling tool developed to calculate the spatial details of the induced structures, an important factor in precise laser machining of surfaces. It furthermore enables to predict and verify assumed physical processes occurring in excited dielectrics. Although the model requires further development (concerning mainly the dynamics of the defect states, their re-excitation during the prolonged irradiation sequence and recombination [22]), it made possible to clarify the origin of crater geometry modulation observed experimentally.

5. Combined thermal/elasto-plastic model: material deformation under femtosecond laser irradiation

The fundamental importance of plasticity has been strikingly demonstrated by fs laser-induced sub-wavelength structuring of thin gold films with formation of microbumps and nanojets/nanobeads [18,19]. However, there are only a few papers concerning the theoretical studies of thermal stresses caused in solids by ultrashort pulsed laser irradiation (see [48,59] and references in them). Post-irradiation stresses can result in irreversible lattice deformations and generation of unusual structures as those obtained in [18,19].

To simulate and analyze the effects involved in microbump and nanojet generation, we use a combination of two modeling approaches [20]. We apply the TTM [5-7] to describe laser energy absorption by free electrons in a thin

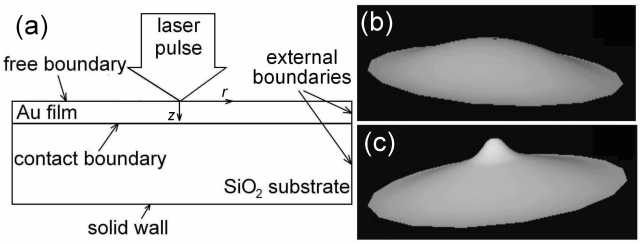

Fig. 12. The computational region (a) and elasto-plastic deformations of the gold film on a quartz substrate at F_0 = 0.94 J/cm^2 (b) and 1.25 J/cm^2 (c) obtained by modeling.

gold film, electron-lattice temperature relaxation, and lattice melting. The temperature gradients obtained by thermal modeling are used as input parameters for the problem of elasto-plastic flow. The latter is solved using the finite element method which allows to model structural deformations of the heated material (see details in [20]). The 2D problem is considered in the cylindrical coordinates implying symmetry of the laser beam whose form was Gaussian both temporally and spatially. All the calculations were performed for a 60-nm thick gold film on a quartz glass substrate irradiated by single laser pulses of 30-fs duration and 800-nm wavelength in the range of laser fluences of 0.94 – 2.04 J/cm^{-2} [60] as in Ref. [19]. The physical properties of gold were taken from Refs. [7,61]. The computational region is illustrated in Fig. 12a. At the free boundary, the external pressure is set to be zero (vacuum conditions above the film). At the contact boundary, if direct contact takes place, the displacements normal to the boundary are equal in the film and in the substrate. If the contact is lost, the pressure below the film is set zero. At the solid wall, the normal displacements are absent and, at the fixed external boundaries, both normal and tangential displacements are equal to zero.

A comment should be made about the adhesive force between the film and the substrate. Here we neglect this force considering it to be small. Indeed, according to Ref. [62], the energy spent for overcoming the adhesion force is in the range of 0.005 – 0.011% of the whole strain energy. Adhesion of a film to a substrate depends on various factors including the technological methods of film deposition. This makes incorrect using in modeling the data on the adhesion force other than for the specific simulated film.

Modeling has uncovered two important aspects. Firstly, the 2D problem of heating the thin film gives the melting threshold fluence well greater as compared to the one-dimensional case. This means that lateral heat flow in the film is considerable even if the film is as thin as 60 nm. We have found that the melting threshold is slightly above of 1.25 J/cm^2 (against 0.8 J/cm^2 for the 1D case). Another important result is that, namely starting from 1.25 J/cm^2, the deformation character of the film in the central part of the irradiation spot changes fundamentally in both modeling [20] and experimental observations [19]. This is illustrated in Fig. 12 where two structures obtained by modeling are given for 0.94 J/cm^2 (b) and 1.25 J/cm^2 (c). At 0.94 J/cm^2 one can se only a bump forming as a result of exfoliation of the film from the substrate. The same structure is obtained under fluences up to 1.2 J/cm^2 while at

around 1.25 J/cm^2 the formation of a structure resembling a jet on the top of the bump takes place (Fig. 12c). This happens because of an absolute loss of film strength when approaching the melting temperature though the film is still solid under such fluence.

For laser fluences above the melting threshold, application of the elasto-plastic model has strong limitations [20]. For the regimes with melting, the calculations with the elasto-plastic model will lead to smaller deformations as compared to actual ones. However, it is obvious that the melted spot appeared in the center of heated zone should continue stretching in the direction normal to the substrate even after stopping the deformation process of the solid part of the film, thus forming the nanojet. Stretching will be stopped finally by the surface tension. The structure called a nanojet should be hollow inside [20]. Indeed simple volumetric considerations indicate that not only microbumps, as found in [19], but also nanojets are hollow structures. To form a solid nanojet ~200 nm in diameter and ~2 μm in length, more material is required than is involved in a structural change (see e.g. Fig. 1 of [19], 1.57 J/cm^2). During stretching, thin nanojet walls can experience hydrodynamic instabilities leading to a wavy character of the final nanojet structure and to bridges inside the jet (a sort of porosity). The destruction of the nanojets at $F \geq 2.5$ J cm^{-2} [19] can be explained by too high momentum gained by the film during deformation at high fluences which can not be extinguished by the surface tension forces.

Gold is a unique material whose plasticity is high and stable for the whole range of temperatures up to the melting point [61]. Namely high plasticity and stability of the mechanical properties over all temperature range (from normal temperature to the melting point) are the necessary conditions for the formation of structures like those obtained in [18,19]. The other important parameters are also the melting temperature, the Young's modulus, and the coefficient of thermal expansion which determine the initial stresses in the film. The higher the values of these parameters are, the greater is the potential mechanical energy gained as a result of the laser pulse action. As a result, greater work should be done in the course of plastic deformations. This suggests particularly that refractory metals are unfit for obtaining the nanojet effect. Analyzing the metallic material properties, we can predict that copper, silver, gold, and lead can fit the needs of film micro- and nanotexturing. It should be noted that the metals should be of high purity as any impurities lead to plasticity dips and the temperature zones of brittleness making metals to be unfit for texturing.

6. Conclusion

We have presented a number of numerical models developed to describe the processes taking place at different time and length scales in the different classes of materials under the irradiation by ultrashort laser pulses. The basis of the models consists of the TTM and the continuum drift-diffusion approach. Being supplemented with the additional assumptions and the equations and sometimes reduced by disregarding a number of processes, they allow to describe a wide range of the phenomena like Coulomb and phase explosions, phase transformations in the irradiated solids, plastic deformations, etc. In many respects the models are qualitative and more sophisticated modeling is requisite for deeper understanding the underlying physics. However, the discussed models represent an efficient tool allowing first insight into puzzling matter behavior under ultrafast heating.

Acknowledgment

The works were partially supported by die Deutsche Forschungsgemeinschaft (DFG-project Ro 2074/5-2), INTAS (Proj. No. 1000013-8949), and RFBR (Proj. No. 05-02-16170).

References

[1] B. N. Chichkov, C. Momma, S. Nolte, F. Von Alvensleben, and A. Tünnermann: Appl. Phys. A, **63**, (1996) 109.
[2] G. Petite, P. Daguzan, S. Guizard, and P. Martin: Nucl. Instr. Meth. B, **107**, (1996) 97.
[3] B.C. Stuart, M.D. Feit, S. Herman, A.M. Rubenchik, B.W. Shore, and M.D. Perry: Phys. Rev. B, **53**, (1996) 1749.
[4] A. Othonos: J. Appl. Phys., **83**, (1998) 1789.
[5] M.I. Kaganov, I.M. Lifshitz., and M.V. Tanatarov: Sov. Phys. JETP, **4**, (1957) 173.
[6] S.I. Anisimov, B. Kapeliovich, and T.L. Perel'man: Sov. Phys. JETP, **39**, (1974) 375.
[7] S.-S.Wellershoff, J.Hohlfeld, J.Güdde, and E.Matthias: Appl. Phys. A, **69**, (1999) S99.
[8] R. Stoian, D. Ashkenasi, A. Rosenfeld, and E.E.B. Campbell: Phys. Rev. B, **62**, (2000) 13167.
[9] M. Henyk, F. Costache, and J. Reif: Appl. Surf. Sci., **186**, (2002) 381.
[10] C. V. Shank, R. Yen, and C. Hirlimann: Phys. Rev. Lett., **51**, (1983) 900.
[11] A. Rousse, C. Rischel, S. Fourmaux, I. Uschmann, S. Sebban, G. Grillon, Ph. Balcou, E. Förster, J.P. Geindre, P. Audebert, J.C. Gauthier, and D. Hulin: Nature, **410**, (2001) 65.
[12] P. Stampfli and K. H. Bennemann: Phys. Rev. B, **49**, (1994) 7299.
[13] R. Kelly and A. Miotello: Nucl. Instr. Meth. B, **122**, (1997) 374.
[14] N.M. Bulgakova and I.M. Bourakov: Appl. Surf. Sci., **197-198**, (2002) 41.
[15] K. Sokolowski-Tinten, J. Bialkowski, A. Cavalleri, D. von der Linde, A. Oparin, J. Meyer-ter-Vehn, and S.I. Anisimov: Phys. Rev. Lett., **81**, (1998) 224.
[16] P. Lorazo, L.J. Lewis, and M. Meunier: Phys. Rev. B, **73**, (2006) 134108.
[17] H. Tamura, T. Kohama, K. Kondo, and M. Yoshida: J. Appl. Phys., **89**, (2001) 3520.
[18] Y. Nakata, T. Okada, and M. Maeda: Jpn. J. Appl. Phys., **42**, (2003) L1452.
[19] F. Korte, J. Koch, B.N. Chichkov: Appl. Phys. A **79**, (2004) 879.
[20] Y.P. Meshcheryakov and N.M. Bulgakova: Appl. Phys. A, **82**, (2006) 363.
[21] N.M. Bulgakova, R. Stoian, A. Rosenfeld, I.V. Hertel, and E.E.B. Campbell: Phys. Rev. B, **69**, (2004) 054102.

[22] I.M. Burakov, N.M. Bulgakova, R. Stoian, A. Rosenfeld, and I.V. Hertel: Appl. Phys. A, **81**, (2005) 1639.
[23] B. Rethfeld, K. Sokolowski–Tinten, D. von der Linde, and S.I. Anisimov: Appl. Phys. A, **79**, (2004) 767.
[24] T.E. Itina, J. Hermann, Ph. Delaporte, and M. Sentis: Thin Solid Films, **453-454**, (2004) 513.
[25] J.P. Colombier, P. Combis, F. Bonneau, R. Le Harzic, and E. Audouard: Phys. Rev. B, **71**, (2005) 165406.
[26] E.M. Logothetis and P. Hartman: Phys. Rev., **187**, (1969) 460.
[27] J. Kanasaki and K. Tanimura: Phys. Rev. B, **66**, (2002) 125320.
[28] N.M. Bulgakova, R. Stoian, A. Rosenfeld, I.V. Hertel, W. Marine, and E.E.B. Campbell: Appl. Phys. A, **81**, (2005) 345.
[29] R. Stoian, A. Rosenfeld, D. Ashkenasi, I.V. Hertel, N.M. Bulgakova, and E.E.B. Campbell: Phys. Rev. Lett., **88**, (2002) 097603.
[30] F. Costache and J. Reif: Thin Solid Films**, 453-454**, (2004) 334.
[31] R. Stoian, A. Rosenfeld, I.V. Hertel, N.M. Bulgakova, and E.E.B. Campbell: Appl. Phys. Lett., **85**, (2004) 694.
[32] N.M. Bulgakova, A.V. Bulgakov, and O.F. Bobrenok: Phys. Rev. E, **62**, (2000) 5624.
[33] W.G. Roeterdink, L.B.F. Juurlink, O.P.H. Vaughan, J. Dura Diez, M. Bonn, and A.W. Kleyn: Appl. Phys. Lett., **82**, (2003) 4190.
[34] H. Dachraoui, W. Husinsky, and G. Betz: Appl. Phys. A, **83**, (2006) 333.
[35] T.Q. Jia, Z.Z. Xu, X.X. Li, R.X. Li, B. Shuai, and F.L. Zhao: Appl. Phys. Lett., **82**, (2003) 4382.
[36] K. Sokolowski-Tinten and D. von der Linde: Phys. Rev. B, **61**, (2000) 2643.
[37] M. Li, S. Menon, J.P. Nibarger, and G.N. Gibson: Phys. Rev. Lett., **82**, (1999) 2394.
[38] D. Ashkenasi, R. Stoian, and A. Rosenfeld: Appl. Surf. Sci., **154-155**, (2000) 40.
[39] F. Quèrè, S. Guizard, P. Martin, G. Petite, O. Gobert, P. Meynadier, and M. Perdrix: Appl. Phys. B, **68**, (1999) 459.
[40] B. Rethfeld, A. Kaiser, M. Vicanek, G. Simon: Phys. Rev. B, 65, 214303 (2002).
[41] V.P. Skripov: "Metastable Liquids" (Halsted Press, New York, 1974).
[42] N.M. Bulgakova and A.V. Bulgakov: Appl. Phys. A, **73**, (2001) 199.
[43] L.V. Zhigelei: Appl. Phys. A, **76**, (2003) 339.
[44] D.S. Ivanov and L.V. Zhigilei: Phys. Rev. B, **68**, (2003) 064114.
[45] H.O. Jeschke and M.E. Garcia, Ultrafast structural changes induced by femtosecond laser pulses, in B.W. Adams (ed.), "Nonlinear Optics, Quantum Optics and Ultrafast Phenomena with X-rays" (Kluwer Academic Publishers, Boston/Dordrecht/London, 2003), pp. 175-214.
[46] M.M. Martynyuk and P.A. Tamanga: High Temp. – High Press., **31**, (1999) 561.
[47] V. Schmidt, W. Husinsky, and G. Betz: Phys. Rev. Lett., **85** (2000) 3516.
[48] J.K. Chen, J.E. Beraun, and C.L. Tham: J. Opt. A: Appl. Opt., **4**, (2002) 650.
[49] K. Furusawa, K. Takahashi, H. Kumagai, K. Midorikawa, and M. Obara: Appl. Phys. A, **69**, (1999) S359.
[50] R. Stoian, A. Mermillod-Blondin, N.M. Bulgakova, A. Rosenfeld, I.V. Hertel, M. Spyridaki, E. Koudoumas, P. Tzanetakis, and C. Fotakis: Appl. Phys. Lett., **87**, (2005) 124105.
[51] D. Perez and L.J. Lewis: Phys. Rev. B: **67**, (2003) 184102.
[52] M.M. Martynyuk and N.Yu. Kravchenko: Appl. Phys., **1**, (2003) 79.
[53] D. Li and P. M. Fauchet: Appl. Phys. Lett. 51, (1987). 1747
[54] N.M. Bulgakova, R. Stoian, A. Rosenfeld, I.V. Hertel, and E.E.B. Campbell: Proc. SPIE, **5714**, (2005) 9.
[55] R. Stoian, M. Boyle, A. Thoss, A. Rosenfeld, G. Korn, and I.V. Hertel: Appl. Phys. A, **77**, (2003) 265.
[56] G. Petite, S. Guizard, Ph. Martin, and F. Quéré: Phys. Rev. Lett., **83**, (1999) 5182.
[57] "Handbook of Physical Quantities" ed. I.S. Grigoryev, E.Z. Meilikhov, and A.A. Radzig (CRP Press, Boca Raton, 1995).
[58] Ya. B. Zeldovich and O.M. Todes: Zhurn. Eksper. Teor. Fiz., **10**, (1940) 1441 (1940) (in Russian).
[59] X. Wang and X. Xu: Appl. Phys. A, **73**, (2001) 107.
[60] In [20], the units of laser fluence should read "J cm^{-2}" everywhere in the text and not "J m^{-2}" as appears in places mistakenly.
[61] G.V. Foss: "Gold" (Gosgeoltechizdat, Moscow 1963) (in Russian).
[62] A.V. Fedenev, E.I. Lipatov, V.F. Tarasenko, V.M. Orlovskii, M.A. Shulepov, N.N. Koval', and I.M. Goncharenko: Quantum Elec., **34**, (2004) 375.

(Received: May 16, 2006, Accepted: February 23, 2007)